Progress In Electromagnetics Research M, Vol. 19, 209–220, 2011

CSAR IMAGING WITH DATA EXTRAPOLATION AND APPROXIMATE GLRT TECHNIQUES

L. Yu[1, 2, *] and Y. Zhang[2]

[1]Graduate University of the Chinese Academy of Sciences, Beijing 100039, China

[2]The Key Laboratory of Microwave Remote Sensing, Chinese Academy of Sciences, Beijing, China

Abstract—Circular synthetic aperture radar (CSAR) is different from other usual SAR modes, e.g., Stripmap SAR or Spotlight SAR, which takes a circular path rather than a straight path. It can provide not only two-dimensional (2-D) high resolution images but also three-dimensional (3-D) information about the target. In this paper, 2-D CSAR imaging containing 3-D information about the target is discussed. Considering the limited bandwidth of radar system and the limited angular persistence of the reflector's scattering characteristic in a real scene, we combine the data extrapolation technique based on the autoregressive (AR) model with the non-coherent combination of the sub-aperture images based on the approximate Generalized Likelihood Ratio Test (GLRT) technique to get a 2-D CSAR image with resolution improved and with aspect-dependent reflectivity characteristics kept. The GTRI T-72 tank dataset is processed to test the algorithm.

1. INTRODUCTION

In circular synthetic aperture radar (CSAR) mode, the radar illuminates the target over a complete 360 degrees aperture [1–3]. The CSAR's wide-angle non-planar collection geometry leads to its unique features: it can realize two-dimensional (2-D) high-resolution imaging as well as possible three-dimensional (3-D) imaging. In this paper, 2-D CSAR imaging containing 3-D information about the target is considered. There exist some problems in the real 2-D imaging application of CSAR. First, due to the limited bandwidth

Received 29 June 2011, Accepted 25 July 2011, Scheduled 3 August 2011

* Corresponding author: Lingjuan Yu (yljsmile@163.com).

of radar system and the limited angular persistence of the reflector's characteristic (few reflectors provide persistent responses larger than 20 degrees [4, 5]), the prefect resolution is hard to be achieved. Second, the traditional imaging algorithms based on the assumption of isotropic scattering may obscure aspect-dependent scattering characteristic of the target. In fact, the first problem can be solved by traditional super-resolution techniques. There are mainly three kinds of super-resolution imaging algorithms, including spectrum estimation (e.g., MUSIC [6], ESPRIT [7]), spectrum extrapolation (e.g., AR model [8–10]) and adaptive weighting methods (e.g., SVA [11, 12]). In this paper, the AR model is adopted to extrapolate phase history data outside the observation area before imaging processing, so it can avoid setting these data to 0. The second problem can be solved by the approximate Generalized Likelihood Ratio Test (GLRT) technique through non-coherently combining the sub-aperture images [13–16], which can effectively keep the aspect-dependent scattering characteristics.

The GTRI dataset for T-72 tank was publicly-released on the Air Force Research Laboratory (AFRL) website in 2006 [17]. These extensive turntable data can be treated as the CSAR data, which have been used in analyzing the principle of CSAR and verifying the imaging algorithm by Soumekh [1, 2]. Considering public release requirements of the military data, the data have been down-sampled in both azimuth aperture and frequency domain. In this paper, we combine the data extrapolation based on the AR model with the non-coherent combination of the sub-aperture images based on the approximate GLRT to form an enhanced 2-D T-72 tank image with aspect-dependent scattering behavior kept.

The rest of this paper is organized as follows. Section 2 briefly introduces the 2-D imaging model of CSAR. Section 3 introduces the data extrapolation technique based on the AR model. Section 4 illustrates the basic idea of composite image based on the approximate GLRT. Section 5 presents the imaging processing and results of GTRI data. Finally, Section 6 concludes the paper.

2. TWO-DIMENSIONAL IMAGING MODEL OF CSAR

The CSAR imaging geometry is shown in Fig. 1(a). Its top view and side view are shown in Figs. 1(b) and (c) respectively. Let's assume the radar locates on the plane $z = z_0$, and the flight radius is R. Then the slant range can be expressed by,

$$R_0 = \sqrt{R^2 + z_0^2} \tag{1}$$

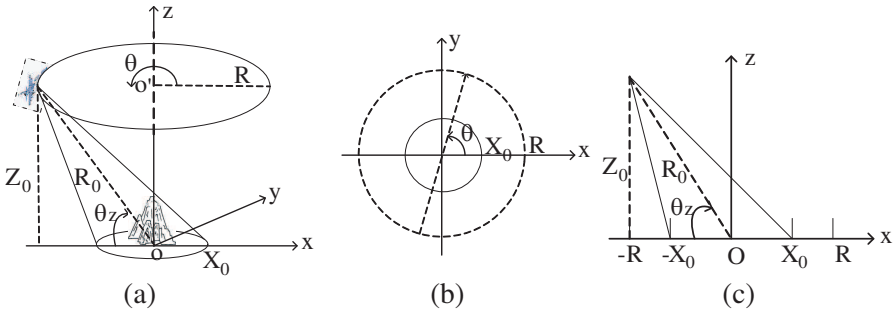

Figure 1. (a) Geometry of CSAR imaging system. (b) Top view. (c) Side view.

and the slant depression angle can be calculated by

$$\theta_z = \arctan\left(\frac{z_0}{R}\right) \tag{2}$$

Let's denote the transmitted radar signal as $p(t)$, and define the reflectivity function of the target on the ground plane $z = 0$ as $f(x, y)$. Then the received echo signal can be given by [1],

$$s(t,\theta) = \int_y \int_x f(x,y) p\left[t - \frac{2\sqrt{(x - R\cos\theta)^2 + (y - R\sin\theta)^2 + z_0^2}}{c}\right] dxdy \tag{3}$$

The Fourier transform of (3) with respect to the fast-time t is,

$$s(\omega,\theta) = P(\omega) \int_y \int_x f(x,y) \exp\left(-j2k\sqrt{(x - R\cos\theta)^2 + (y - R\sin\theta)^2 + z_0^2}\right) dxdy \tag{4}$$

where ω denotes the fast-time frequency, θ denotes the aspect angle, $P(\omega)$ denotes the Fourier transform of $p(t)$, $k = \frac{\omega}{c}$, and $c = 3 \times 10^8$ m/s.

The above signal model is based on the assumption that the target locates on the ground plane $z = 0$. In practice, the target has a varying height as the variation of (x, y). If we define the height function as $z(x, y)$, then the model (3) can be modified as [1],

$$s(t,\theta) = \int_y \int_x f(x,y,z(x,y)) p\left[t - \frac{2\sqrt{(x - R\cos\theta)^2 + (y - R\sin\theta)^2 + (z(x,y) - z_0)^2}}{c}\right] dxdy \tag{5}$$

After imaging processing at the imaging (focus) plane $z = z_h$, the 2-D imaging result can be denoted as $I(x, y, z_h)$, which contains the 3-D information about the target. Specifically, $I(x, y, 0)$ corresponds to the focus ground plane of $z = 0$. When $|z_h| \ll R_0$, the image $I(x, y, z_h)$ at any focus plane can be deduced from $I(x, y, 0)$ by using [15, 16],

$$I(x, y, z_h) = \mathbb{F}_{x,y}^{-1}\left[\mathbb{F}_{x,y}\left[I(x, y, 0)\right] \exp\left(-j\sqrt{k_x^2 + k_y^2}\tan\theta_z z_h\right)\right] \quad (6)$$

where $\begin{cases} k_x = \frac{\omega}{c}\cos\theta_z\cos\theta \\ k_y = \frac{\omega}{c}\cos\theta_z\sin\theta \end{cases}$.

3. DATA EXTRAPOLATION BASED ON THE AR MODEL

In this section, the principle of one-dimensional data extrapolation based on the AR model is discussed firstly, and then two kinds of data extrapolation schemes are introduced.

Let $\{x(n), n = 1, 2, \ldots N\}$ be the observation data. The forward prediction of $x(n)$ based on the p-th order AR model can be defined by [8, 9],

$$\hat{x}_f^p(n) = -\sum_{i=1}^{p} a_i x(n-i) \quad (7)$$

and the backward prediction can be done via

$$\hat{x}_b^p(n-p) = -\sum_{i=1}^{p} b_i x(n-p+i) \quad (8)$$

The forward prediction error can be expressed as,

$$e_f^p(n) = x(n) - \hat{x}_f^p(n) = x(n) + \sum_{i=1}^{p} a_i x(n-i) \quad (9)$$

and the backward prediction error can be expressed as,

$$e_b^p(n) = x(n-p) - \hat{x}_b^p(n-p) = x(n-p) + \sum_{i=1}^{p} a_i^* x(n-p+i) \quad (10)$$

where a_i denotes the i-th filter coefficient, $b_i = a_i^*$, and $n = p+1, p+2, \ldots, N$.

Once the order p is fixed, the coefficients of a_i and b_i in the AR model can be obtained through the minimization of $\{\frac{1}{2}\sum_{n=p+1}^{N}(|e_f^p(n)|^2 + |e_b^p(n)|^2)\}$.

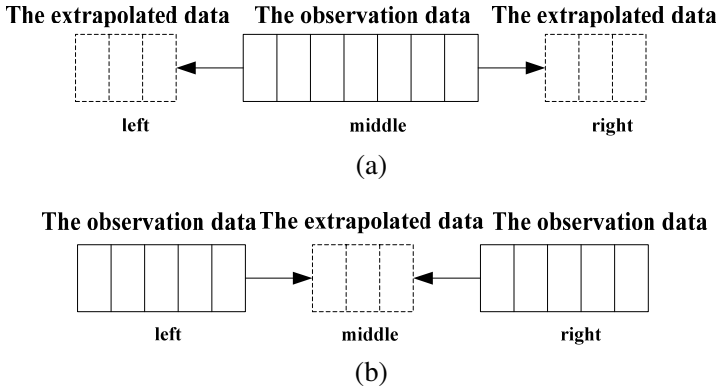

Figure 2. Data extrapolation. (a) Scheme 1. (b) Scheme 2

Next, we shall introduce two schemes for data extrapolation based on the AR model, which will be used in Section 5.

Scheme 1: As shown in Fig. 2(a), one group of the observation data is used in extrapolating the data on the left and right sides. In this case, after obtaining the AR model coefficients, the right side data can be calculated by (7), and the left side data can be calculated by (8).

Scheme 2: As shown in Fig. 2(b), two groups of the observation data are used in extrapolating data in the middle. In this case, we first calculate the AR model coefficients of one group of the observation data on the left side, and extrapolate them to obtain the middle data $\hat{x}_R(n)$ through (7). Secondly, we calculate the AR model coefficients of the other group of the observation data on the right side, and extrapolate them to obtain the middle data $\hat{x}_L(n)$ through (8). Finally, we combine $\hat{x}_R(n)$ with $\hat{x}_L(n)$ using the weighted coefficients to obtain the final middle data.

4. COMPOSITE IMAGE BASED ON THE APPROXIMATE GLRT

Because of the limited visible angle range of scatterers, full-aperture imaging will obscure aspect-dependent reflectivity characteristic, which means a large amplitude response persisting over a small angle extent may become a low amplitude average response over the full 360 degrees azimuth aperture. The approximate GLRT is one of the efficient ways to solve this problem by non-coherently combining the sub-aperture images [13–16].

On the basis of Section 2, we divide the echo data into M

subapertures. When the focus plane of $z = 0$ is chosen, the m-th sub-aperture image can be constructed by [15, 16]

$$I_m(x, y, 0) = \mathbb{F}_{x,y}^{-1}\left[F\left(k_x, k_y, \sqrt{k_x^2+k_y^2}\tan\theta_z\right)W_m(\tan^{-1}(k_x/k_y))\right] \quad (11)$$

where $F(k_x, k_y, \sqrt{k_x^2 + k_y^2}\tan\theta_z)$ denotes the Fourier transform of the reflectivity function $f(x, y, z(x, y))$, and the azimuthal window function $W_m(\theta)$ is given by,

$$W_m(\theta) = \begin{cases} W\left(\frac{\theta-\theta_m}{\Delta}\right), & -\frac{\Delta}{2} < \theta < \frac{\Delta}{2} \\ 0, & \text{otherwise} \end{cases} \quad (12)$$

where θ_m denotes the center azimuth angle for the m-th window, and Δ denotes the width of window.

By substituting (11) into (6), we can obtain a 2-D sub-aperture image $I_m(x, y, z_h)$ at the focus plane $z = z_h$.

The basic principle of approximate GLRT is to take the non-coherent maximum over the sub-aperture images. So, the final composite image $I_G(x, y, z_h)$ can be obtained by [15, 16],

$$I_G(x, y, z_h) = \max_m |I_m(x, y, z_h)| \quad (13)$$

5. IMAGING PROCESSING OF THE GTRI T-72 TANK DATA

5.1. Description of the GTRI T-72 Tank Data

As described on the AFRL website [17], the basic information about the GTRI T-72 tank data is as follows:

(1) It provides full-polarization phase history data with center frequency of 9.6 GHz.

(2) There are totally 29 folders in the released dataset, and each folder corresponds to a depression angle. There are 85 data files for each polarization in each folder, which means that the full-aperture data is divided into 85 subapertures.

(3) Each data file contains 221 complex frequency samples by 79 complex azimuth samples after being down-sampled.

(4) The frequency step is 3 MHz, the aspect angle step is 0.05 degrees, and the depression angle step is 0.138 degrees.

From the above information, we can deduce that the bandwidth is about $(221 - 1) \times 3 = 660$ MHz, and there are about $(360/85 - 79 \times 0.05) \approx 0.2853$ degrees of azimuthal data are missing in each data file (for each subaperture).

In the following imaging processing, the data of folder f115 with a depression angle of 29.9994 degrees will be used. We choose the focus plane of $z = 0.75\,\mathrm{m}$, which corresponds to the relative height of the cannon of the T-72 tank [1]. It should be emphasized that the zero-Doppler clutter must be removed from the phase history data before the imaging processing [18].

5.2. Azimuthal Data Extrapolation Based on the AR Model

The HH polarization data over the full-aperture in the folder f115 are used here. The data extrapolation in azimuth aperture can

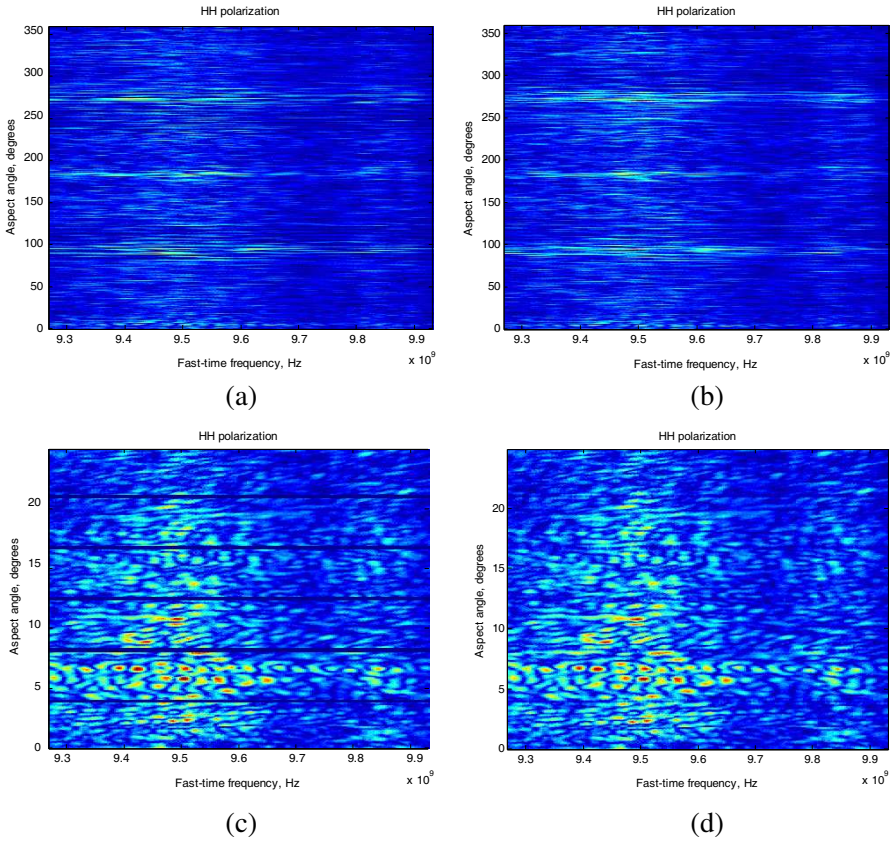

Figure 3. Phase history data (a) without extrapolation in azimuth aperture, (b) with extrapolation in azimuth aperture, (c) a zoomed in part of (a), (d) a zoomed in part of (b).

be implemented in the way of scheme 2 as described in Section 3. Fig. 3(a) and Fig. 3(b) show the phase history data before and after extrapolation in azimuth, respectively. A zoomed in part of Fig. 3(a) is shown in Fig. 3(c). It is obvious that there are some gaps between subapertures before data extrapolation. However, the gaps are successfully filled after data extrapolation as shown in Fig. 3(d).

5.3. Fast-time Frequency Data Extrapolation Based on the AR Model

After the data extrapolation in azimuthal direction, the data extrapolation in the fast-time frequency domain can be implemented in the way of scheme 1 as described in Section 3. The full-aperture phase history data after extrapolation is shown in Fig. 4(a). A zoomed in part of Fig. 4(a) is shown in Fig. 4(b). As a result, the signal bandwidth of 660 MHz has been extended to 1.2 GHz.

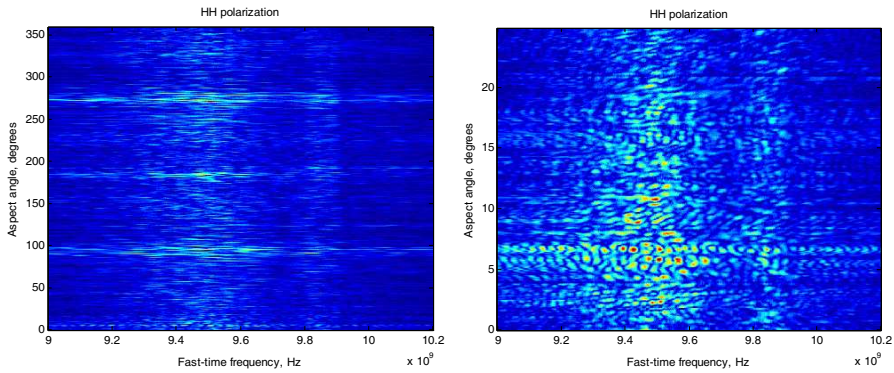

(a) (b)

Figure 4. Phase history data (a) after extrapolation (both in azimuth aperture and frequency domain), (b) a zoomed in part of (a).

5.4. Composite Image Based on the Approximate GLRT

In view of the fact that most of the scatterers of T-72 tank are anisotropic over the full-aperture, the approximate GLRT technique can be used to non-coherently combine all the 85 sub-aperture images. For comparison purpose, coherent combination of sub-aperture images is also implemented.

After choosing the focus plane of $z = 0.75$ m, we use the back propagation (BP) algorithm for the 2-D sub-aperture imaging. The

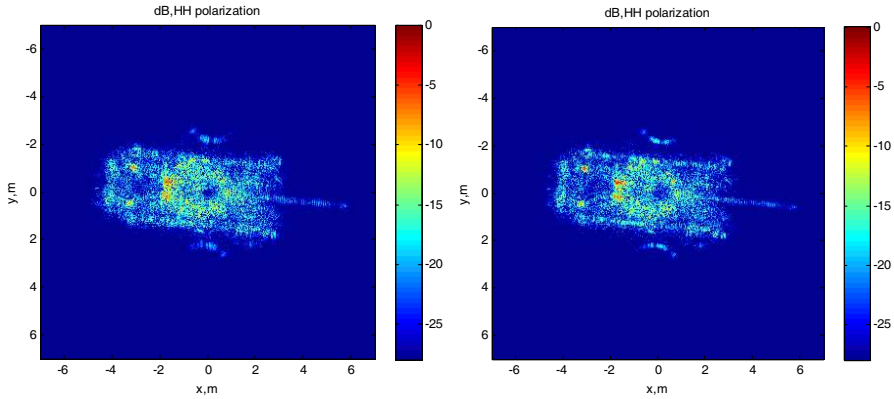

(a) (b)

Figure 5. Coherent combination of the sub-aperture images (a) without extrapolation, (b) with extrapolation.

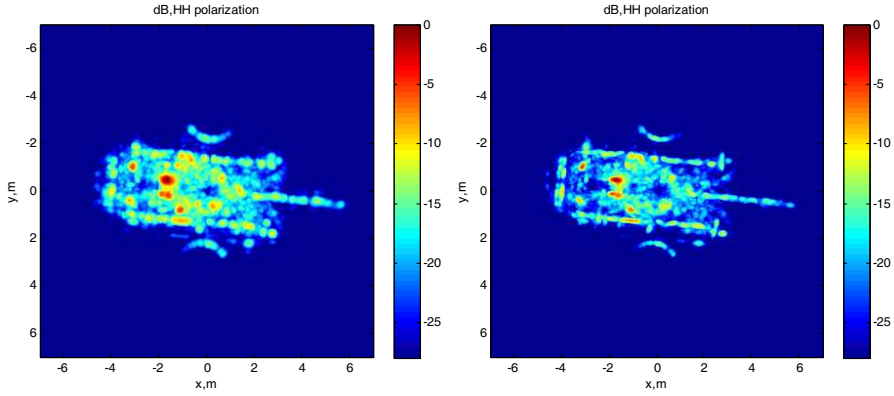

(a) (b)

Figure 6. Non-coherent combination of the sub-aperture images based on the approximate GLRT (a) without extrapolation, (b) with extrapolation.

composite images based on the coherent combination of sub-aperture images before and after data extrapolation are shown in Fig. 5(a) and Fig. 5(b), respectively. The composite images based on the approximate GLRT technique before and after data extrapolation are shown in Fig. 6(a) and Fig. 6(b), respectively. Meanwhile, Fig. 7 shows the serial number of subaperture (azimuth angle, indicated by the color

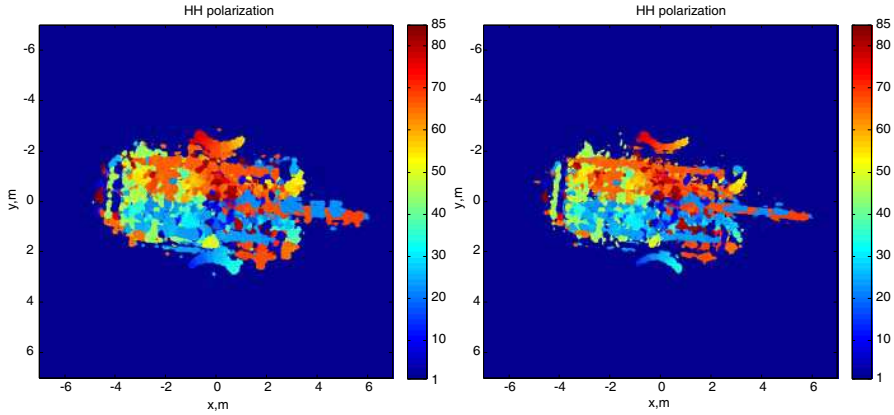

(a) (b)

Figure 7. (a) The serial number of subaperture (azimuth angle, indicated by the color bar) corresponds to each pixel in Fig. 6(a), (b) the serial number of subaperture (azimuth angle, indicated by the color bar) corresponds to each pixel in Fig. 6(b).

bar) corresponding to each pixel in Fig. 6.

From Fig. 5 and Fig. 6, one can see that the cannon of the T-72 tank is well focused due to the right focus plane is chosen, while the two corner reflectors appear to be defocused because they are not located on the same height as the cannon is. Therefore, we can also get 3-D information from these 2-D images.

By comparing Fig. 5(a) with Fig. 6(a), and Fig. 5(b) with Fig. 6(b), one can see that some scatterers with large scattering amplitude persisting over a narrow range of aspect angles finally possess small amplitude in the coherently combined images. But with the non-coherent combination of the sub-aperture images based on the approximate GLRT, the large scattering amplitude of scatterers can be well maintained. From Fig. 7, one can also see the serial number of subaperture (azimuth angle) corresponding to the maximum amplitude of each pixel in these 2-D imaging results.

After comparing Fig. 5(a) with Fig. 5(b), one can see that the resolution is improved significantly after data extrapolation in the coherently composite image. At the same time, comparing Fig. 6(a) with Fig. 6(b), one can see that the resolution is also remarkably enhanced after data extrapolation in the non-coherently combined image based on the approximate GLRT technique.

6. CONCLUSION

In this paper, the AR model is applied to extrapolating the GTRI T-72 tank data both in the fast-time frequency domain and in the circular aperture direction. Imaging results show that the resolution is improved significantly after data extrapolation. At the same time, non-coherent combination of sub-aperture images based on the approximate GLRT technique is performed to further improve the imaging quality. The results indicate that the aspect-dependent scattering characteristic of each scatterer can be well kept.

REFERENCES

1. Soumekh, M., *Synthetic Aperture Radar Signal Processing with Matlab Algorithms*, Ch. 7, Wiley, New York, 1999.
2. Soumekh, M., "Reconnaissance with slant plane circular SAR imaging," *IEEE Trans. Image Process.*, Vol. 5, No. 8, 1252–1265, Aug. 1996.
3. Ishimaru, A., T. Chan, and Y. Kuga, "An imaging technique using confocal circular synthetic aperture radar," *IEEE Trans. Geosci. Remote Sens.*, Vol. 36, No. 5, 1524–1530, Sep. 1998.
4. Dudgeon, D. E., R. T. Lacoss, C. H. Lazott, et al., "Use of persistant scatterers for model-based recognition," *Proc. SPIE 2230*, 356–368, Apr. 1994.
5. Trintinalia, L. C., R. Bhalla, and H. Ling, "Scattering center parameterization of wide-angle backscattered data using adaptive gaussian representation," *IEEE Trans. Antennas and Propagation*, Vol. 45, 1664–1668, Nov. 1997.
6. Odendaal, J. W., E. Barnard, and C. W. I Pistorius, "Two-dimensional superresolution radar imaging using the MUSIC algorithm," *IEEE Trans. Antennas and Propagation*, Vol. 42, No. 10, 1386–1391, 1994.
7. Roy, R. and T. Kailath, "ESPRIT-estimation of signal parameters via rotational invariance techniques," *IEEE Transactions on Acoustics, Speech and Signal Processing*, Vol. 37, No. 7, 984–995, 1989.
8. Gupta, I. J., M. J. Beals, and A. Moghaddar, "Data extrapolation for high resolution radar imaging," *IEEE Trans. Antennas and Propagation*, Vol. 42, No. 11, 1540–1545, 1994.
9. Kayran, A. H. and I. Erer, "Optimum asymmetric half-plane autoregressvie lattice parameter modeling of 2-D fields," *IEEE Trans. Signal Processing*, Vol. 52, No. 3, 807–819, 2004.

10. Yu, L.-J. and Y.-H. Zhang, "One-dimensional spectrum extrapolation for circular SAR imaging," *International Symposium on Antennas Propagation and EM Theory*, Nov. 2010.
11. Stankwitz, H. C., R. J. Dallaire, and J. R. Fienup, "Nonlinear apodization for sidelobe control in SAR imagery," *IEEE Transactions on Aerospace and Electronic Systems*, Vol. 31, No. 1, 267–279, 1995.
12. Zhai, W. and Y. Zhang, "Application of super-sva to stepped-chirp radar imaging with frequency band gaps between subchirps," *Progress In Electromagnetics Research B*, Vol. 30, 71–82, 2011.
13. Moses, R. L. and L. C. Potter, "Noncoherent 2D and 3D SAR reconstruction from wide-angle measurements," *13th Annual Adaptive Sensor Array Processing Workshop*, MIT Lincoln Laboratory, Lexington, MA, Jun. 2005.
14. Moses, R. L., E. Ertin, and C. Austin, "Synthetic aperture radar visualization," *Proceedings of the 38th Asilomar Conference on Signals, Systems, and Computers*, Pacific Grove, CA, Nov. 2004.
15. Ertin, E., L. C. Potter, and R. L. Moses, "Enhanced imaging over complete circular apertures," *Proceedings of the 40th Asilomar Conference on Signals, Systems, and Computers*, Nov. 2006.
16. Ertin, E., R. L. Moses, and L. C. Potter, "Interferometric methods for three-dimensional target reconstruction with multipass circular SAR," *Radar, Sonar and Navigation, IET*, Vol. 4, No. 3, 464–473, 2010.
17. GTRI-dataset website: https://www.sdms.afrl.af.mil/datasets/g-tri.
18. Showman, G. A., M. A. Richards, and K. J. Sangston, "Comparison of two algorithms for correcting zero-Doppler clutter in turntable ISAR imagery," *Proceedings of the 32th Asilomar Conference on Signals, Systems, and Computers*, Nov. 1998.